Journal of Physics and Chemistry of Solids 172 (2023) 111063

Contents lists available at ScienceDirect

Journal of Physics and Chemistry of Solids

journal homepage: www.elsevier.com/locate/jpcs

New modulated structures induced by electron beam irradiation in $SrCrO_3$ single crystal

Minghui Xu [a,b], Lipeng Cao [a], Weipeng Wang [a], Yifan Ding [a,b], Xi Shen [a,*], Yuan Yao [a], Changqing Jin [a,b], Richeng Yu [a,b,c,**]

[a] Beijing National Laboratory of Condensed Matter Physics, Institute of Physics, Chinese Academy of Sciences, P. O. Box 603, Beijing, 100190, PR China
[b] School of Physical Sciences, University of Chinese Academy of Sciences, Beijing, 100190, PR China
[c] Songshan Lake Materials Laboratory, Dongguan, Guangdong, 523808, PR China

ARTICLE INFO

Keywords:
Modulated structures
Electron beam irradiation
Transmission electron microscopy
Scanning transmission electron microscopy
Ab initio calculations

ABSTRACT

Three new modulated structures induced by controllable electron beam irradiation (EBI) were obtained from $SrCrO_3$ single crystal. The crystal and electronic structures were investigated using aberration-corrected scanning transmission electron microscopy, electron energy loss spectroscopy (EELS) and *ab initio* calculations. The EELS results revealed that EBI induced ordered oxygen vacancies and generated modulated structures $SrCrO_{2.5}$ (*I4/mmm*), $SrCrO_{2.8}$ (*C2/m*) and $SrCrO_{2.67}$ (*C2/m*) from pristine $SrCrO_3$ (*Pmm*). The corresponding structural models were proposed and modified by *ab initio* calculations. Additionally, the electronic structures of the optimized modulated structures were further investigated.

1. Introduction

The transition metal oxides, e.g. $ACr^{4+}O_3$ (A = Sr, Ca and Ba), have recently attracted considerable attention because of their characteristic properties induced by the partially filled *d* shell of the Cr ion and the strong electron–lattice coupling effect [1–7]. Among them, pristine $SrCrO_3$ exhibits a cubic structure with $Cr^{4+}O_6$ octahedra. Due to the fluctuation of Cr^{4+} valence, $SrCrO_3$ can only be synthesized under extreme conditions of high pressure and high temperature. Previous works indicated that $SrCrO_3$ has a ferromagnetic transition at 50 K and a structural phase transition from a cubic to an orthorhombic structure below 100 K [8]. Ortega-San-Martin et al. reported that polycrystalline $SrCrO_3$ had a phase separation induced by lattice strain at low temperature, which includes an original paramagnetic cubic phase and an antiferromagnetic tetragonal phase [5]. However, some results indicated that $SrCrO_3$ does not undergo magnetic transformation at low temperature [9]. In addition, cubic $SrCrO_3$ can be reversibly transformed into rhombohedral $SrCrO_{2.8}$ under artificially controlled experimental conditions [10], and at 400–500 °C by using redox reactions [11]. Ong et al. explored the formation of oxygen vacancies and the collective mass transport in an epitaxial $SrCrO_{3-\delta}$ thin film based on *ab initio* calculations [12]. They believed that processes of fast mass transport give importance to some functional materials in which fast O^{2-} transport occurs, such as solid oxide fuel cells and electrochemical reactors [10,12]. However, there is also some debate about the electrical properties of $SrCrO_3$. It was reported that $SrCrO_3$ displays metallic behavior in temperature-dependent resistivity measurements [8], and infrared observations [13]; however, it displayed semiconducting behavior in temperature-dependent resistivity measurements [14,15]. Zhou et al. found that polycrystalline $SrCrO_3$ is in a metallic state at pressures exceeding 4 GPa, but showed nonmagnetic insulating behavior at ambient pressure [4]. Therefore, the ground state of $SrCrO_3$ needs to be discussed further [16].

The electronic, transport and magnetic properties can be modified by external fields, such as temperature, hydrogenation, strain and electron beam irradiation (EBI) [17–25]. The EBI can induce a structural transition by relaxing unstable bonds or generating oxygen vacancies more precisely compared with thermal annealing [21–23,26,27]. For example, the unit cell volume of $LaMnO_{3.15}$ slightly expands with increasing EBI dosage [28].

In this work, we report that EBI induced three kinds of modulated structures from $SrCrO_3$ single crystal. We used aberration-corrected

* Corresponding author.
** Corresponding author. Beijing National Laboratory of Condensed Matter Physics, Institute of Physics, Chinese Academy of Sciences, P. O. Box 603, Beijing, 100190, PR China.
E-mail addresses: xshen@iphy.ac.cn (X. Shen), rcyu@iphy.ac.cn (R. Yu).

https://doi.org/10.1016/j.jpcs.2022.111063
Received 8 March 2022; Received in revised form 18 October 2022; Accepted 19 October 2022
Available online 2 November 2022

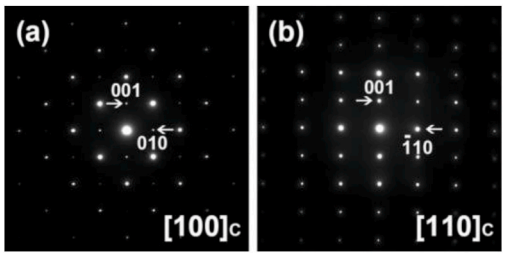

Fig. 1. SAED patterns of pristine $SrCrO_3$ single crystal along the (a) $[100]_C$ and (b) $[110]_C$ zone axes.

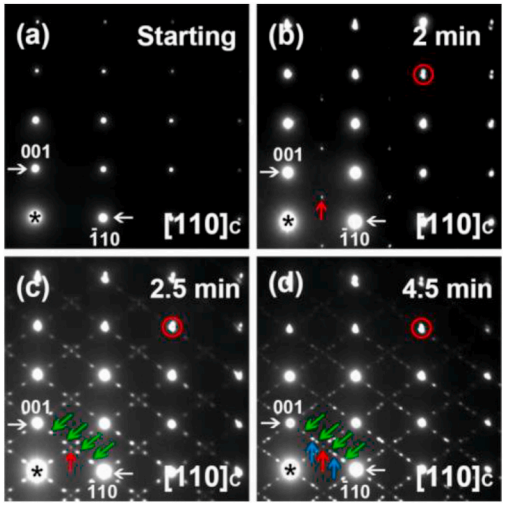

Fig. 2. The SAED patterns of the $SrCrO_3$ single crystal along the $[110]_C$ zone axis, recorded (a) at the beginning of irradiation experiment and after irradiation of (b) 2 min, (c) 2.5 min and (d) 4.5 min.

scanning transmission electron microscopy (STEM) and electron energy-loss spectroscopy (EELS) to study the crystal and electronic structures of these new superstructures. We also explored the origin of the modulated structures and constructed the corresponding structural models. We optimized the models using first-principles calculations and carried out simulation works of electron diffraction and STEM images to justify the rationality of the models. The calculated energy bands and density of states (DOS) of the pristine phase and three kinds of modulated phases were further investigated. The EBI-induced modulated structures of transition metal oxides may have novel properties and potential applications.

2. Experimental sections

2.1. Preparation of samples

A single crystal $SrCrO_3$ was synthesized by utilizing SrO and CrO_2 as primary materials under 5.5 GPa and 500 °C. The synthesis details as well as the transport and magnetic properties of the sample were previously described [9]. The specimens for transmission electron microscopy (TEM) observations were prepared by focused ion beam technology. All the samples and TEM specimens were stored in a glove box filled with Ar gas at 1 atm pressure to avoid contamination from air and water.

2.2. Characterization

The STEM [high-angle annular dark-field (HAADF) and annular bright-field (ABF)], EELS and selected area electron diffraction (SAED) were performed on a JEM-ARM200F microscope with double Cs correctors for the condenser lens and objective lens. The available point resolution was better than 0.078 nm at an operating voltage of 200 kV. The acceptance angles were 90–370 mrad for HAADF imaging and 11.5–23 mrad for ABF imaging. All EELS spectra were collected in image mode in case of an orientation effect. The lattice constants and internal coordinates of the pristine and modulated structures were optimized by *ab initio* calculations based on density functional theory using the CASTEP program, which was also used to calculate energy bands and DOS.

3. Results and discussion

3.1. TEM irradiation analysis

The TEM results showed that the pristine $SrCrO_3$ single crystal had a cubic structure with lattice constants of $a_p \times a_p \times a_p$ (space group *Pmm*)

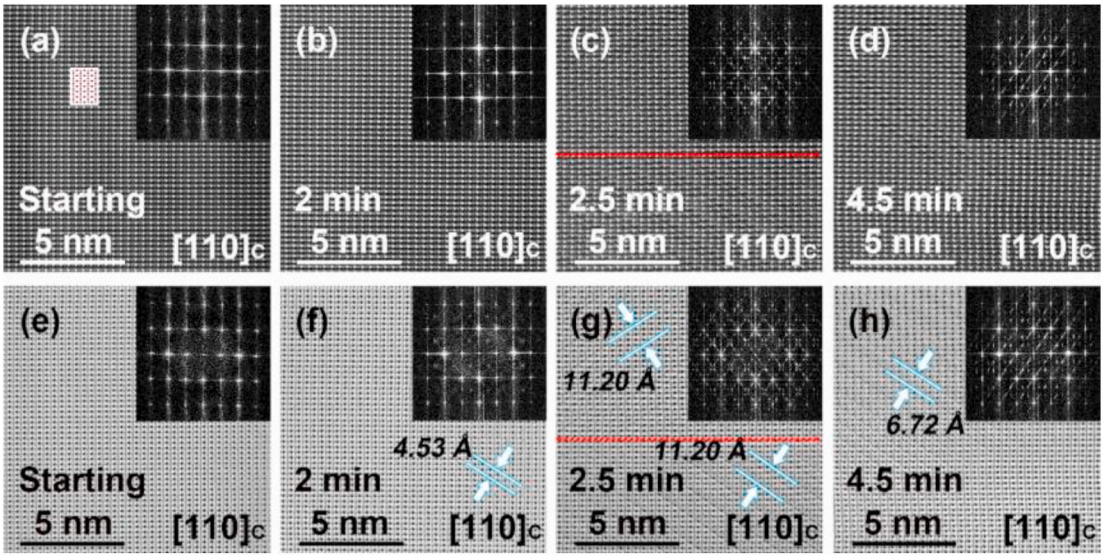

Fig. 3. STEM HAADF images of the $SrCrO_3$ single crystal along the $[110]_C$ zone axis (a) before irradiation (inset is the projection of structural model) and after irradiation of (b) 2 min, (c) 2.5 min and (d) 4.5 min. The corresponding STEM ABF images along the $[110]_C$ zone axis (e) before irradiation and after irradiation of (f) 2 min, (g) 2.5 min (h) and 4.5 min (insets are the corresponding FFT patterns).

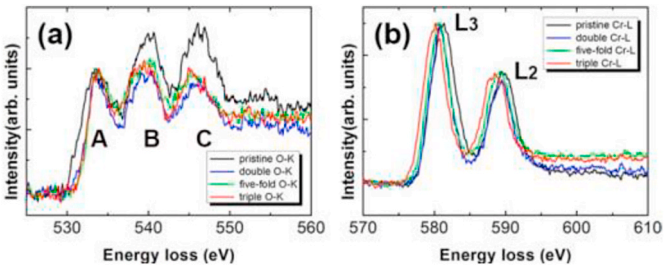

Fig. 4. The EELS spectra with fine structures of the pristine (black line) $SrCrO_3$ and double (red line), five-fold (blue line) and triple (green line) modulation structures: (a) O–K edges and (b) Co $L_{2,3}$ edges.

under 200 keV when the EBI dose rate was relatively low. Some obvious extra electron diffraction spots appeared when the dose rate increased to 40.1 pA/cm^2 for the specimen region with a relative specimen thickness of 0.25λ (λ is the mean free path of $SrCrO_3$ [29]). Keeping the dose rate of 40.1 pA/cm^2, we studied the EBI effect on the pristine $SrCrO_3$. Fig. 1 illustrates a cubic structure of pristine $SrCrO_3$ recorded at the beginning of the irradiation, consistent with a previous report [9]. Fig. 2 displays the evolution behavior of the SAED patterns of $SrCrO_3$ with increasing irradiation time along the $[110]_C$ zone axis (subscript C denotes the primitive cubic phase). After irradiation of 2 min, extra reflection spots (marked by red arrows) appeared in {111}*-reciprocal planes (Fig. 2b) in contrast with the fundamental perovskite reflection spots (Fig. 2a). It should be noted that additional reflection spots appeared at the middle position of the basic spots along the $[111]^*_C$ direction, indicating a doubled unit cell along this direction. With increasing irradiation time, new extra reflection spots (marked by green arrows) appeared along the $[111]^*_C$ direction and divided the basic reciprocal vector into five equal parts, implying a five-fold unit cell along this direction (Fig. 2c). With further irradiation, new reflection spots (marked by blue arrows) occurred at the 1/3 position of basic spots along the $[111]^*_C$ direction, showing a triple unit cell along this direction (Fig. 2d). It should also be noted that there was no change in the electron diffraction pattern along the $[100]_C$ zone axis during irradiation. The extra diffraction spots induced by EBI imply the formation of lower symmetry structures, as shown by the splitting of the spots (red circles, Fig. 2b–d), which came from both the pristine phase and modulated phases. Hereafter, we name these modulated structures double, five-fold and triple modulated structures, respectively. We also performed EBI on different regions and observed the same phenomenon.

3.2. STEM irradiation analysis

Typical STEM HAADF, ABF images and corresponding fast Fourier transform (FFT) patterns before and after EBI along the $[110]_C$ axis are presented in Fig. 3. The FFT patterns in Fig. 3b and f reveal the presence of modulated structure after irradiation of 2 min. Fig. 3c and g shows that "stripes" appeared and formed some domain structures (indicated by the red dotted line) after irradiation of 2.5 min. The corresponding FFT patterns indicated the existence of five-fold modulation structure. Meanwhile, the narrower "stripes" and corresponding extra spots in FFT occurred after irradiation of 4.5 min and remained stable in the further EBI (Fig. 3d and h), indicating the existence of triple modulated structure. We also studied the evolution behavior under EBI for specimens of different thicknesses and observed that the thinner the observed area, the faster the evolution proceeds. As the relative thickness changed from 0.25λ to 0.42λ, for instance, the dose rate required for the occurrence of the modulated structure needed to increase from 40.1 to 240 pA/cm^2. Moreover, the stronger the dose rate, the quicker the modulation structures formed.

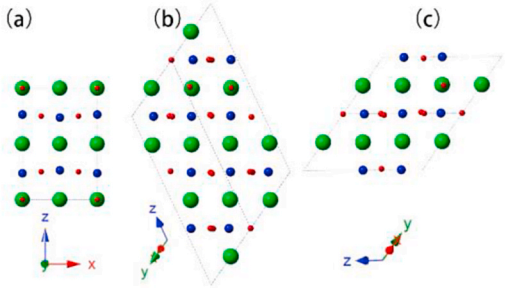

Fig. 5. The projection of the optimized structural models of (a) $SrCrO_{2.5}$, (b) $SrCrO_{2.8}$ and (c) $SrCrO_{2.67}$ along the $[110]_C$ zone axis. The green, blue and red balls represent Sr, Cr and O atoms, respectively.

3.3. EELS analysis

To reveal the origin of the modulated structures induced by EBI, we performed EELS line scan investigations on the specimen before and after EBI. The TEM EELS is a powerful tool to determine the valence states of transition metals in high spatial resolution. Fig. 4a and b displays EELS line scan core-loss spectra of O–K and Cr-$L_{2,3}$ absorption edges before and after EBI, respectively. The fine structure of the O–K edge derived from the electron transition from O 1*s* to 2*p* bands. The A, B and C in Fig. 4a represent the maxima of spectra originating from the hybridization between O and Cr ions, O and Sr ions, and O and Sr, Cr ions, respectively [30]. Normalizing the intensity of peak A showed that the intensities of both peaks B and C from the modulated structures were significantly lower than that from the pristine structure. In addition, the energy separation between peaks A and B became progressively smaller in five-fold, triple and double modulation structures compared with the pristine $SrCrO_3$ due to their progressively lower oxygen content [31]. Similarly, Cr-$L_{2,3}$ spectra were normalized by L_3 intensity. The L_2 and L_3 edges were produced by the excitation of electrons from the spin–orbit coupling split orbitals $2p_{1/2}$ and $2p_{3/2}$ to the partially occupied 3*d* orbital, respectively. With increasing valence from Cr(II) to Cr(VI), not only did Cr-$L_{2,3}$ edges have a systematic shift to the higher energy side, but the intensity ratio of L_3/L_2 decreased [32]. In our results, the chemical shifts of the L_3 peak were about 0.7, 1.0 and 1.3 eV for double, five-fold and triple modulation structures, respectively (Fig. 4b). In addition, the intensity ratio of L_3/L_2 decreased in the order of double, triple, five-fold and pristine structures, confirming that modulated structures had lower Cr valences compared with the pristine structure. Since no extra cation (Sr or Cr) was doped into the crystal, the decreasing of Cr valence was induced by the loss of oxygen generated by EBI. As a consequence, the origin of the modulated structures can be explained as follows: EBI prompted perovskite $SrCrO_3$ to lose different oxygen contents at different stages and led to forming ordered oxygen vacancies, giving rise to the phase transition from the cubic structure to the modulated structures. The mechanism of the structural evolution is similar to that previously reported [26].

It should be noted that the modulated structures induced by irradiation were almost irreversible. Only slow recovery of the original structure was detected in a slightly irradiated sample. This phenomenon will happen when the modulated structure with ordered oxygen vacancies absorbs surrounding or airborne oxygen atoms. A slow re-oxidation of $SrCrO_{3-\delta}$ phases to $SrCrO_3$ was observed after five months at room temperature on exposure to small amounts of air [11].

3.4. Ab initio calculations

Based on the TEM results, we constructed three oxygen-deficient ordered modulated structures and optimized them using *ab initio* calculations. The composition of double, five-fold and triple modulation structures were stoichiometric $SrCrO_{2.5}$, $SrCrO_{2.8}$ and $SrCrO_{2.67}$,

Table 1
The optimized supercell parameters and coordinates of the crystal structures of $SrCrO_{2.5}$, $SrCrO_{2.8}$ and $SrCrO_{2.67}$. The space groups of the superstructures are *I*4/*mmm*, *C*2/*m* and *C*2/*m*, respectively.

	a(Å)	*b*(Å)	*c*(Å)	label	x	y	z
$SrCrO_{2.5}$	5.3413	5.3413	7.9111	Sr(1)	0.5000	1.000000	0.00000
				Cr(2)	0.5000	0.5000	0.73647
				O(3)	1.0000	1.0000	0.0000
				O(4)	0.2500	0.7500	0.7500
$SrCrO_{2.8}$	9.4599	5.4033	16.7197	Sr(1)	0.79700	0.50000	0.59680
				Sr(2)	0.39320	0.50000	0.79400
				Sr(3)	0.50000	0.00000	0.00000
				Cr(4)	0.50000	0.00000	0.50000
				Cr(5)	0.59740	0.50000	0.69800
				Cr(6)	0.17200	0.50000	0.89050
				O(7)	0.67040	0.75810	0.81050
				O(8)	0.45780	0.24970	0.40210
				O(9)	0.25000	0.25000	0.00000
				O(10)	0.89120	0.50000	0.79570
				O(11)	0.30600	0.50000	0.60900
$SrCrO_{2.67}$	9.5118	5.3843	11.6150	Sr(1)	0.50330	0.00000	0.33499
				Sr(2)	0.50000	0.00000	0.00000
				Cr(3)	0.50000	0.50000	0.50000
				Cr(4)	0.00225	0.00000	0.17917
				O(5)	0.75582	0.24432	0.68172
				O(6)	0.25000	0.75000	0.00000
				O(7)	0.52249	0.50000	0.35180

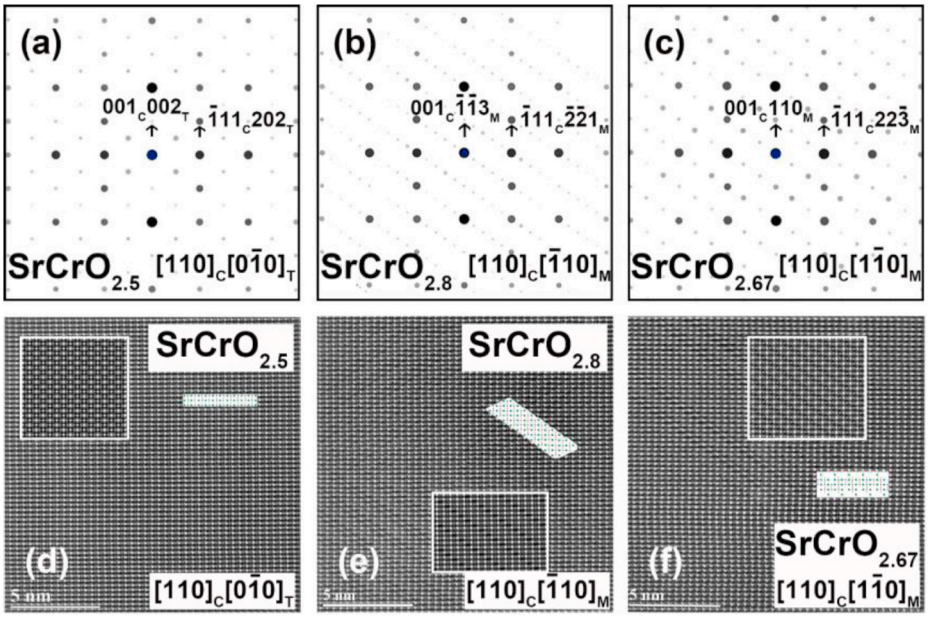

Fig. 6. Simulated SAED patterns of (a) $SrCrO_{2.5}$, (b) $SrCrO_{2.8}$ and (c) $SrCrO_{2.67}$ along the $[0\ \bar{1}\ 0]_T$, $[\bar{1}1\ 0]_M$ and $[1\ \bar{1}\ 0]_M$ axes (corresponding to the $[110]_C$ axis of the cubic structure), respectively. The corresponding experimental HAADF images of (d) $SrCrO_{2.5}$, (e) $SrCrO_{2.8}$ and (f) $SrCrO_{2.67}$ along the $[110]_C$ zone axis, the insets are the corresponding simulated HAADF images and the projection of structural models.

respectively. Their supercells are redefined. The $[110]_C$ zone axis of primitive cubic $SrCrO_3$ is the $[0\ \bar{1}\ 0]_T$ zone axis of $SrCrO_{2.5}$, $[\bar{1}1\ 0]_M$ zone axis of $SrCrO_{2.8}$ and $[1\ \bar{1}\ 0]_M$ zone axis of $SrCrO_{2.67}$. The subscript T and M denote the tetragonal and monoclinic phases, respectively. The modulated structural models along the $[110]_C$ axis produced by VESTA software [33] are shown in Fig. 5, and the unit cell parameters and coordinates of the optimized superstructures are listed in Table 1. Among the three modulation structures, the component $SrCrO_{2.8}$ is the same as reported by Arévalo-López et al. [11]. According to their X-ray and neutron diffraction results, they believed that $SrCrO_{2.8}$ had a rhombohedral structure with a space group $R\bar{3}m$. However, we selected a different supercell in calculation according to the SAED and HAADF results. Our results indicated that the five-fold modulated phase $SrCrO_{2.8}$ had a monoclinic structure with a space group *C*2/*m*.

The optimized structures were used to simulate SAED patterns and ABF images (Fig. 6). The simulated SAED patterns (Fig. 6a–c) matched well with the experimental SAED patterns (Fig. 2b–d). Moreover, the qualitative agreements between the simulated and experimental HAADF images (Fig. 6d–f) suggested the rationality of the superstructures. It should be noted that an orthorhombic structure $SrCrO_3$ (space group *Imma*, $a_O = 5.3997$, $b_O = 7.6052$ and $c_O = 5.3944$ Å) was reported on account of the slight compression of CrO_6 octahedron under 100 K [8]. We also optimized this orthorhombic structure using *ab initio* calculations and found that it was not dynamically stable.

Furthermore, we calculated the energy band structures and DOS using *ab initio* calculations. To reduce calculation complexity, we transformed the lattice unit cells of $SrCrO_{2.5}$, $SrCrO_{2.8}$ and $SrCrO_{2.67}$ to their corresponding primitive cells in this calculation. Fig. 7a and b

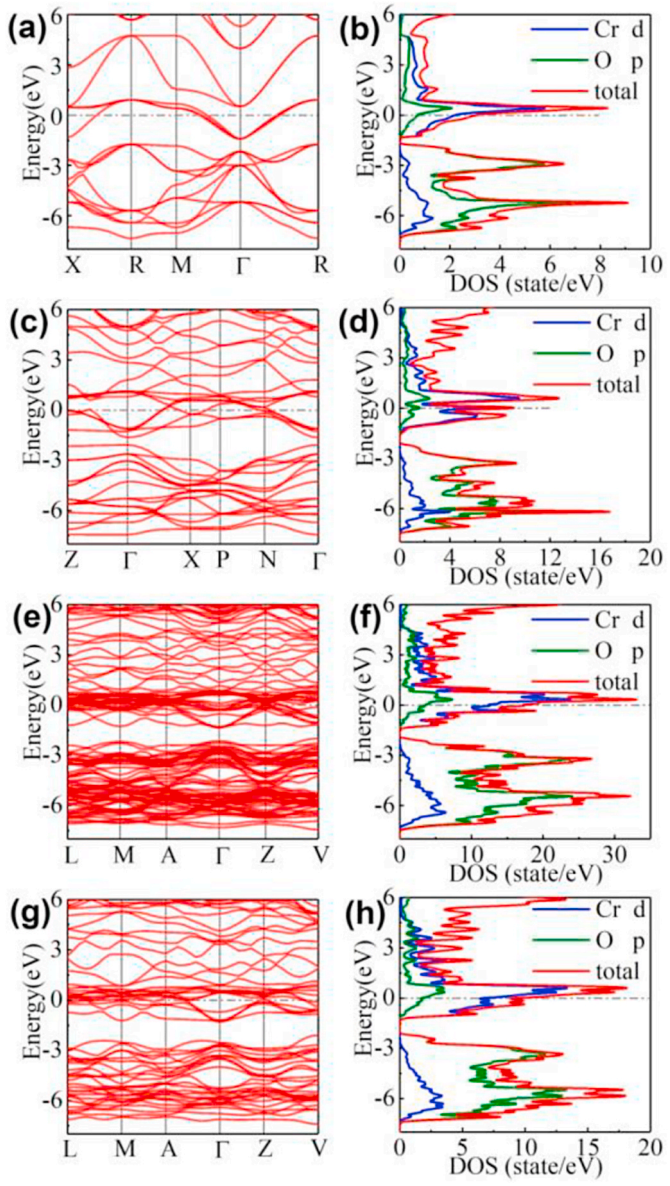

Fig. 7. The energy band structure and DOS of (a, b) $SrCrO_3$, (c, d) $SrCrO_{2.5}$, (e, f) $SrCrO_{2.8}$ and (g, h) $SrCrO_{2.67}$.

presents the calculated energy band structures and DOS of $SrCrO_3$. The DOS and partial DOS (Fig. 7b) showed that the main contributions to the Fermi level were O-2*p* and Cr-3*d* electrons and there was strong hybridization between O-2*p* and Cr-3*d* electrons. Combined with the corresponding energy band structures in Fig. 7a, the Fermi level clearly crossed the energy band, implying metallicity. Fig. 7c–h shows the energy band structures and DOS of irradiation-induced modulated structure $SrCrO_{2.5}$, $SrCrO_{2.8}$ and $SrCrO_{2.67}$. Similarly, these modulated structures also had metallic characteristics. In addition, the primitive cells of $SrCrO_3$, $SrCrO_{2.5}$ ($Sr_2Cr_2O_5$), $SrCrO_{2.8}$ ($Sr_5Cr_5O_{14}$) and $SrCrO_{2.67}$ ($Sr_3Cr_3O_8$) showed that the increased number of nonequivalent atomic positions in a primitive cell should induce the degenerate energy levels to form splitting states. These characteristics were indicated by the crowded energy levels in our calculated band structures (Fig. 7).

We used thermodynamics to study the propensity of the transformation from the pristine phase $SrCrO_3$ to double modulated phase $SrCrO_{2.5}$, five-fold modulated phase $SrCrO_{2.8}$ and triple modulated phase $SrCrO_{2.67}$ during EBI. To characterize the thermodynamic stability of the SCO system, we introduced the formation energy of oxygen vacancies at 0 K: $E_{V_O}^{form} = \frac{1}{\delta}E_{SrCrO_{3-\delta}} + 1/2E_{O_2} - \frac{1}{\delta}E_{SrCrO_3}$ [34], where $E_{V_O}^{form}$ is the energy of forming an oxygen vacancy in $SrCrO_3$, $E_{SrCrO_{3-\delta}}$ is the cell energy with δ oxygen vacancies, E_{SrCrO_3} is the cell energy without oxygen vacancy and E_{O_2} is the Gibbs free energy approximation of a gaseous oxygen molecule at 0 K. According to these calculations, the $E_{V_O}^{form}$ of $SrCrO_{2.5}$, $SrCrO_{2.67}$ and $SrCrO_{2.8}$ were 4.78, 4.64 and 4.61 eV, respectively. This indicates that the order of the forming energies in the SCO system was $E_{SrCrO_{2.5}}$ $E_{SrCrO_{2.67}}$ $E_{SrCrO_{2.8}}$, which does not coincide exactly with the observed occurrence order of the modulated phases. The reason may be that the formation of the modulated phases is not only based on the initial and final states, but also closely related to the barrier height, i.e. thermodynamics and kinetics, as also found by Park et al. [35]. In addition, because $SrCrO_{2.5}$, $SrCrO_{2.8}$ and $SrCrO_{2.67}$ have similar energies, under external fields such as EBI, the three phases can probably transform into each other and/or coexist. This is consistent with our experimental results.

4. Conclusions

In summary, three kinds of modulated structures formed in cubic $SrCrO_3$ under EBI. Our TEM studies showed that the superstructures were caused by the ordered oxygen vacancies. The oxygen-deficient ordered structural models of $SrCrO_{2.5}$, $SrCrO_{2.8}$ and $SrCrO_{2.67}$ were constructed and optimized using *ab initio* calculations. The agreements between the experimental and simulated results implied the rationality of the superstructures. In addition, we further calculated the energy bands and DOS of the optimized structural structures using *ab initio* calculations, and found that both the pristine phase and the modulated phases were metallic. The calculation results verified that the phase transformation of $SrCrO_3$ under EBI was dynamically stable. Our results also indicate that EBI can be used to generate oxygen vacancies in some functional materials to optimize utilization.

Credit author statement

Minghui Xu performed the TEM experiments and wrote the original draft with input from all authors, **Lipeng Cao** prepared the samples under high pressure, **Weipeng Wang** performed the STEM experiments, **Yifan Ding** performed the theoretical calculations, **Xi Shen** performed the STEM experiments, proposed and supervised the overall research work, **Yuan Yao** reviewed the manuscript and suggested improvements, **Changqing Jin** reviewed the manuscript and suggested improvements, **Richeng Yu** revised the draft, proposed and supervised the overall research work.

Declaration of competing interest

The authors declare that they have no known competing financial interests or personal relationships that could have appeared to influence the work reported in this paper.

Data availability

Data will be made available on request.

Acknowledgements

This work was supported by the National Key Research Program of China (Grant Nos. 2022YFA1402801 and 2018YFA0208402), the National Natural Science Foundation of China (Grant Nos. 11874413, 11934017 and 51972333) and the Strategic Priority Research Program of the Chinese Academy of Sciences (Grant No. XDB33030200). X. Shen is grateful for the support from the Youth Innovation Promotion Association of Chinese Academy of Sciences (Grant No. 2019009).

References

[1] M.S. Dyer, C. Collins, D. Hodgeman, P.A. Chater, A. Demont, S. Romani, R. Sayers, M.F. Thomas, J.B. Claridge, G.R. Darling, M.J. Rosseinsky, Computationally assisted identification of functional inorganic materials, Science 340 (2013) 847–852.

[2] K.G. Sanjaya Ranmohotti, E. Josepha, J. Choi, J.X. Zhang, J.B. Wiley, Topochemical manipulation of perovskites: low-temperature reaction strategies for directing structure and properties, Adv. Mater. 23 (2011) 442–460.

[3] J.B. Goodenough, Electronic and ionic transport properties and other physical aspects of perovskites, Rep. Prog. Phys. 67 (2004) 1915–1993.

[4] J.S. Zhou, C.Q. Jin, Y.W. Long, L.X. Yang, J.B. Goodenough, Anomalous electronic state in $CaCrO_3$ and $SrCrO_3$, Phys. Rev. Lett. 96 (2006), 046408.

[5] L. Ortega-San-Martin, A.J. Williams, J. Rodgers, J.P. Attfield, G. Heymann, H. Huppertz, Microstrain sensitivity of orbital and electronic phase separation in $SrCrO_3$, Phys. Rev. Lett. 99 (2007), 255701.

[6] S.Q. Luo, J.F. Wang, B. Yang, Y. Yuan, Recent advances in controlling the crystallization of two-dimensional perovskites for optoelectronic device, Front. Physiol. 14 (2019), 53401.

[7] T.-H. Han, S. Tan, J. Xue, L. Meng, J.-W. Lee, Y. Yang, Interface and defect engineering for metal halide perovskite optoelectronic devices, Adv. Mater. 31 (2019), 1803515.

[8] A.J. Williams, A. Gillies, J.P. Attfield, G. Heymann, H. Huppertz, M.J. Martínez-Lope, J.A. Alonso, Charge transfer and antiferromagnetic insulator phase in $SrRu_{1-x}Cr_xO_3$ perovskites: solid solutions between two itinerant electron oxides, Phys. Rev. B 73 (2006), 104409.

[9] L.P. Cao, L.Q. Pan, W.M. Li, X.C. Wang, Q.Q. Liu, Y.W. Long, C.Z. Gu, C.Q. Jin, High pressure growth and characterization of $SrCrO_3$ single crystal, Int. J. Mod. Phys. B 29 (2015), 1542025.

[10] K.H.L. Zhang, P.V. Sushko, R. Colby, Y. Du, M.E. Bowden, S.A. Chambers, Reversible nano-structuring of $SrCrO_{3-\delta}$ through oxidation and reduction at low temperature, Nat. Commun. 5 (2014) 4669.

[11] A.M. Arévalo-López, J. Rodgers, M.S. Senn, F. Sher, J. Farnham, W. Gibbs, J. P. Attfield, Hard-soft" synthesis of $SrCrO_{3-\delta}$ superstructure phases, Angew. Chem. Int. Ed. 51 (2012) 10791–10794.

[12] P.-V. Ong, Y. Du, P.V. Sushko, Low-dimensional oxygen vacancy ordering and diffusion in $SrCrO_{3-\delta}$, J. Phys. Chem. Lett. 8 (2017) 1757–1763.

[13] A.C. Komarek, T. Möller, M. Isobe, Y. Drees, H. Ulbrich, M. Azuma, M. T. Fernández-Díaz, A. Senyshyn, M. Hoelzel, G. André, Y. Ueda, M. Grüninger, M. Braden, Magnetic order, transport and infrared optical properties in the $ACrO_3$ system (A = Ca, Sr, and Pb), Phys. Rev. B 84 (2011), 125114.

[14] E. Castillo-Martínez, A.M. Arévalo-López, R. Ruiz-Bustos, M.A. Alario-Franco, Increasing the structural complexity of chromium(IV) oxides by high-pressure and high-temperature reactions of CrO_2, Inorg. Chem. 47 (2008) 8526–8542.

[15] E. Castillo-Martínez, M.Á. Alario-Franco, Revisiting the Sr-Cr(IV)-O system at high pressure and temperature with special reference to $Sr_3Cr_2O_7$, Solid State Sci. 9 (2007) 564–573.

[16] B.L. Chamberland, Preparation and properties of $SrCrO_3$, Solid State Commun. 5 (1967) 663.

[17] J.H. Markna, R.N. Parmar, D.G. Kuberkar, Ravi Kumar, D.S. Rana, S.K. Malik, Thickness dependent swift heavy ion irradiation effects on electronic transport of $(La_{0.5}Pr_{0.2})Ba_{0.3}MnO_3$ thin films, Appl. Phys. Lett. 88 (2006), 152503.

[18] R.N. Parmar, J.H. Markna, D.G. Kuberkar, Swift-heavy-ion-irradiation-induced enhancement in electrical conductivity of chemical solution deposited $La_{0.7}Ba_{0.3}MnO_3$ thin films, Appl. Phys. Lett. 89 (2006), 202506.

[19] V.V. Efimov, E.A. Efimova, K. Iakoubovskii, D.V. Karpinskii, S. Khasanov, D. I. Kochubey, V.V. Kriventsov, A. Kuzmin, A.P. Sazonov, V. Sikolenko, M. Sakharov, A.N. Shmakov, S.I. Tiutiunnikov, Effect of high-current pulsed electron beam irradiation on the structure of $La_{0.7}Sr_{0.3}CoO_3$ powder, J. Phys. Chem. Solid. 67 (2006) 2001–2006.

[20] M.H. Xu, L.P. Cao, W.P. Wang, Y.F. Ding, X. Shen, Y. Yao, C.Q. Jin, R.C. Yu, Study on structural stability of $SrCrO_3$ under electron beam irradiation, J. Chin. Electr. Microsc. Soc. 37 (2018) 226–231.

[21] M. Takashiri, K. Imai, M. Uyama, H. Hagino, S. Tanaka, K. Miyazaki, Y. Nishi, Effects of homogeneous irradiation of electron beam on crystal growth and thermoelectric properties of nanocrystalline bismuth selenium telluride thin films, J. Alloys Compd. 612 (2014) 98–102.

[22] S. Chattopadhyay, A. Sarkar, A. Banerjee, S. Karmakar, D. Banerjee, R. Kumar, B. K. Chaudhuri, Effect of Li^{3+} irradiation on the transport properties of $La_{0.7}Pb_{0.3}MnO_3$ type CMR material, Nucl. Instrum. Methods Phys. Res. B 226 (2004) 274–280.

[23] S. Chattopadhyay, S. Pal, A. Sarkar, R. Kumar, B.K. Chaudhuri, Radiation damage effects in CMR manganite materials, Nucl. Instrum. Methods Phys. Res. B 230 (2005) 274–278.

[24] T. Jia, P. Ohodnicki, B. Chorpening, J. Lekse, G. Hackett, Y. Duan, Theoretical study of the optical and thermodynamic properties of $La_xS.r_{1-x}Co_{1-y}Fe_yO3-\delta$ (x/y = 0.25, 0.5, 0.75) perovskites, Phys. Chem. Chem. Phys. 21 (2019) 26117–26122.

[25] M. Wu, S. Chen, C. Huang, X. Ye, H. Zhou, X. Huang, K.H.L. Zhang, W. Yan, L. Zhang, K. Kim, Modulation of the electronic states of perovskite $SrCrO_3$ thin films through protonation via low-energy hydrogen plasma implantation approaches, Front. Physiol. 15 (2020), 13601.

[26] L. Yao, S. Majumdar, L. Äkäslompolo, S. Inkinen, Q.H. Qin, S.V. Dijken, Transition metal oxides: electron-beam-induced Perovskite-Brownmillerite-Perovskite structural phase transitions in epitaxial $La_{2/3}Sr_{1/3}MnO_3$ films, Adv. Mater. 26 (2014) 2789–2793.

[27] B.L. Belevtsev, V.B. Krasovitsky, V.V. Bobkov, D.G. Naugle, K.D.D. Rathnayaka, A. Parasiris, Influence of high-energy electron irradiation on the transport properties of $La_{1-x}Ca_xMnO_3$ films ($x \approx 1/3$), Eur. Phys. J. B 15 (2000) 461–468.

[28] B. Christopher, A. Rao, G.S. Okram, V. Chandra, V. Pal, J. Dwivedi, Comprehensive study on effect of electron beam irradiation on electrical, thermo-electric and magnetic properties of oxygen rich $LaMnO_{3.15}$ compound, J. Alloys Compd. 703 (2017) 216–224.

[29] R.F. Egerton, Electron Energy Loss Spectroscopy in the Electron Microscope, second ed., Plenum Press, New York, 1986.

[30] A.M. Arévalo-López, E. Castillo-Martínez, M.Á. Alario-Franco, Electron energy loss spectroscopy in $ACrO_3$ (A = Ca, Sr and Pb) perovskites, J. Phys. Condens. Matter 20 (2008), 505207.

[31] M. Varela, M. Oxley, W. Luo, J. Tao, M. Watanabe, A. Lupini, S. Pantelides, S. Pennycook, Atomic-resolution imaging of oxidation states in manganites, Phys. Rev. B 79 (2009), 085117.

[32] T.L. Daultona, B.J. Little, Determination of chromium valence over the range Cr(0)-Cr(VI) by electron energy loss spectroscopy, Ultramicroscopy 106 (2006) 561–573.

[33] K. Momma, F. Izumi, *VESTA 3* for three-dimensional visualization of crystal, volumetric and morphology data, J. Appl. Crystallogr. 44 (2011) 1272–1276.

[34] Y. Tang, H. Zhang, L. Cui, C. Ouyang, S. Shi, W. Tang, H. Li, J.-S. Lee, L. Chen, First-principles investigation on redox properties of M-doped CeO_2 (M = Mn, Pr, Sn, Zr), Phys. Rev. B 82 (2010), 125104.

[35] J. Park, Y.N. Wu, W.A. Saidi, B. Chorpening, Y. Duan, First-principles exploration of oxygen vacancy impact on electronic and optical properties of $ABO_{3-\delta}$ (A = La, Sr; B = Cr, Mn) perovskites, Phys. Chem. Chem. Phys. 22 (2020), 27163.